Available online at www.sciencedirect.com

ScienceDirect

journal homepage: www.elsevier.com/locate/he

$CuO/ZnO/TiO_2$ photocathodes for a self-sustaining photocell: Efficient solar energy conversion without external bias and under visible light

Ulugbek Shaislamov [a], *Hyun Kim* [b], *Jun Mo Yang* [c], *Bee Lyong Yang* [b,*]

[a] *National University of Uzbekistan, Department of Physics, 100214, Tashkent, Uzbekistan*
[b] *Kumoh National Institute of Technology, School of Materials Science and Engineering, Gumi, 730-701, Republic of Korea*
[c] *Nano-Convergence Technology Division, National Nanofab Center, 291 Daehak-ro, Yuseong-gu, Daejeon city 34141, Republic of Korea*

HIGHLIGHTS

- Double electrode cell was proposed for unassisted H_2 generation by water splitting.
- Photocorrosion of the CuO was addressed by coating with a ZnO/TiO_2 protective layer.
- *p*-CuO/ZnO/TiO_2 and n-TiO_2/CdS/CdSe photoelectrodes forms suitable band alignment.
- Built in potential in *p*-CuO/ZnO/TiO_2 electrode contributes to the charge separation.

GRAPHICAL ABSTRACT

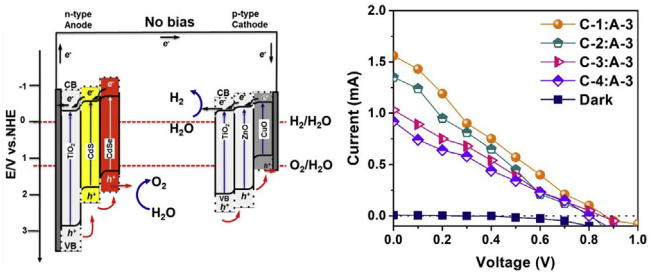

ARTICLE INFO

Article history:
Received 30 August 2019
Received in revised form
4 November 2019
Accepted 9 December 2019
Available online 7 January 2020

ABSTRACT

We report the results of a *p*-CuO nanoflake photocathode combined with an n-type TiO_2 nanorod-based photoanode in a solar-water-splitting photocell, operating without external bias under visible light illumination. Both *p*-CuO nanoflakes and n-TiO_2 nanorods were successfully fabricated by a low-cost solution-based method on transparent conductive substrates. Photocorrosion of the CuO electrode was suppressed by coating with a 200-nm ZnO/TiO_2 protective film, which demonstrated a stability of over 70%. The visible-light response of single crystalline n-TiO_2 nanorods was enhanced by sensitization with CdS/CdSe nanoparticles. Finally, the two n- and p-type photoelectrodes were short-circuited in the photocell, and their current-voltage (I–V) characteristics evaluated under visible-light illumination. The results of the I–V measurements reveal that the performance of the photocell strongly depends on the electrochemical properties of each electrode. The photocell comprising highly stable *p*-CuO and visible-light-active n-TiO_2-based

* *Corresponding author.*
E-mail address: blyang@kumoh.ac.kr (B.L. Yang).
https://doi.org/10.1016/j.ijhydene.2019.12.052

photoelectrodes operating without external bias demonstrated a short-circuit current and photoconversion efficiency of ~1 mA and 0.57%, respectively, under visible-light illumination.

Introduction

Solar hydrogen generation by water splitting is considered a promising technology for providing a source of clean energy. There have been many extensive studies on the development of suitable photocatalyst materials for solar water-splitting in a photoelectrochemical cell (PEC) [1,2]. Generally, conventional PEC cells consist of an n-type or p-type semiconductor photoelectrode and a platinum (Pt) counter electrode. Photo-excited electron-hole pairs in the photoelectrode are involved in water oxidation and reduction process; namely, holes oxidize the water to oxygen on the semiconductor surface, and electrons reduce the water to hydrogen on the counter electrode. Almost all PEC cells require application of an external bias to obtain an effective charge separation and overcome the resistance between the electrodes. The application of an external bias is not desirable from an economical or environmental point of view. Therefore, it would be very beneficial to develop a PEC system that does not require an external bias to trigger a water-splitting reaction. There are several approaches to achieve water splitting in the PEC without external bias, such as using a tandem cell [3–8], a Z-scheme [9–11], and a PEC cell with combined p- and n-type semiconductor photoelectrodes [12–15]. In the tandem cell, the required bias is usually provided by a solar cell. F. F. Abdi achieved a solar to hydrogen efficiency of 4.9% with a tandem cell comprising a $BiVO_4$ metal-oxide semiconductor photoanode and an amorphous Si solar cell [6]. Water splitting in the Z-scheme (or dual photoexcitation) relies on the combined operation of two n-type semiconductors. Basically, in the Z-scheme, one semiconductor with a band position suitable for water oxidation and another for water reduction are placed in a cell containing a suitable redox medium [16]. This method allows the utilization of a wide range of visible-light-responsive photocatalyst materials, ultimately increasing the efficiency of the system. Many studies have been conducted on the Z-scheme using mainly powdered photocatalysts. Recently, H. S. Park has reported water splitting with modified Pt–W/Mo–$BiVO_4$ and $Zn_{0.2}Cd_{0.8}Se$ semiconductor photoelectrodes with I^-/IO_3^- and S^{2-}/S_n^{2-} redox couples [11].

Another promising approach for unbiased water splitting in a PEC cell is the use of a short-circuited n-type photoanode and p-type photocathode. One of advantages of the PEC cell over the tandem cell and Z-scheme is the simplicity of design in the photocatalytic system. Also a built-in potential between n-type photoanode and p-type photocathode in the PEC cell contributes to charge separation of excited electrons and holes in each electrode. Akikusa et al. has demonstrated the possibility of combined operation of p-SiC and n-TiO_2 photoelectrodes under ultraviolet (UV)-light illumination [14]. The photoconversion efficiency of the system was 0.06%, owing to the large band gap energies of the photoelectrodes. Recently Ito et al. have also reported the successful synthesis of a visible-light-active p-$CaFe_2O_4$ photocathode and its combined operation with n-TiO_2 in an unbiased PEC cell [12]. The poor performance of the photocell comprising p-$CaFe_2O_4$ and n-TiO_2 photoelectrodes was attributed to partial decomposition of the $CaFe_2O_4$ electrode in the electrolyte during the operation period. Therefore, the development of stable visible-light-active photoelectrodes with low fabrication cost will further enhance the efficiency of the unbiased PEC cells. There has been extensive research on efficient n-type semiconductor photoelectrodes that are suitable for solar water-splitting. However, the development of stable and visible-light-active p-type photoelectrodes still remains a challenge.

In this work, we demonstrate the possibility of constructing a self-sustaining photocell composed of p-type CuO nanoflake and n-type TiO_2-nanorod photoelectrodes that were prepared by low-cost solution-based methods on transparent fluorine-doped tin oxide (FTO) glass substrates. The n-type TiO_2 electrode was sensitized with CdS/CdSe to enhance its visible-light response. The photocorrosion of the CuO [17,18] photocathode was significantly suppressed by coating with a ZnO/TiO_2 protecting layer. The effect of the protecting layer thickness on the efficiency of the photocell was discussed. It was found that the efficiency of the photocell greatly depended on the photocatalytic properties of the individual employed photoelectrodes. It is significant that the results of this work would contribute to the further development of the solar-hydrogen generation systems operating under visible-light illumination without external bias.

Experimental details

TiO_2 nanorod based photoelectrode

Vertically aligned single-crystalline TiO_2 nanorods on FTO glass substrate were fabricated by a hydrothermal method. In a typical experiment, FTO glass substrates were ultrasonically cleaned with trichloroethylene, acetone, and methanol, and finally dried under N_2 stream. Then, FTO glass substrates were placed into an autoclave containing 30 ml HCl, 30 ml deionized (DI) water, and 1 ml of titanium butoxide solution. The hydrothermal reaction was conducted at 150 °C for 5 h. After the reaction, the samples were thoroughly washed in DI water, dried, and subsequently annealed at 450 °C for 1 h. The TiO_2-nanorod photoelectrode was sensitized with CdS and CdSe nanoparticles by using the successive ionic layer absorption and reaction (SILAR) method [19–22]. For CdS sensitization, the TiO_2-nanorod electrode was first immersed in aqueous 0.1 M $Cd(NO_3)_2$ then in 0.1 M Na_2S solutions and kept in each solution for 3 min. After each immersion, samples were thoroughly rinsed with DI water and dried under an N_2

stream. CdSe nanoparticles were sensitized according to the method described in Ref. [19], where SeO_2 was used as a Se source. The process was repeated several cycles to obtain a desirable nanoparticle density on the TiO_2 surface.

CuO-nanoflake-based photoelectrode

CuO nanostructures on FTO glass substrates were hydrothermally grown in two steps. First, a CuO seed layer was deposited by spin-coating on pre-cleaned FTO 10 times, with the use of an ethanolic solution of 0.01 M $Cu(CH_3COO)_2 \cdot H_2O$. After each coating, samples were dried on a hot plate at 250 °C. Subsequently, the CuO seed layer was crystalized by annealing at 250 °C for 2 h. Next, the FTO glass with CuO seed layer was placed into a glass beaker containing an aqueous solution of 25 mM $(Cu(NO_3)_2 \cdot 3H_2O)$ and 25 mM hexamethylenetetramine (HMTA, $C_6H_{12}N_4$). The hydrothermal reaction was also conducted in two steps. In the first step, reaction was conducted at 90 °C in a conventional oven for 3 h and then annealed at 550 °C. The hydrothermal reaction was then performed for another 2 h, followed by annealing at 550 °C. This, two-step hydrothermal process was done in order to obtain a dense and high-quality CuO film.

ZnO/TiO_2 protecting thin film

ZnO layer was prepared by spin coating the solution of 0.5 M of zinc acetate $(Zn(O_2CCH_3)_2)$ in ethanol onto CuO electrode at 3000 RPM for 30 s which was subsequently heat-treated at 300 °C. A coating solution for TiO_2 film was prepared by mixing 100 ml of ethanol with 6.8 ml Ti-butoxide, 5 ml Acetic acid, 0.36 ml H_2O and 1 drop of tritonx-100. The prepared solution was spin coated at 3000 rpm for 30 s and annealed at 550 °C.

Characterizations

Morphology and microstructural characterizations of the nanostructured samples were performed by using field-emission scanning electron microscopy (FE-SEM) (JSM-6500F) and transmission electron microscopy (TEM) (JEM 2100). Electrochemical measurements were performed by a potentiostat (AMT VERSASTAT3) using a three-electrode configuration system consisting of a Pt-wire counter electrode and a saturated Ag/AgCl reference electrode in 0.1 M KOH electrolyte for CuO and 0.1 M Na_2S for TiO_2-based electrodes. A working electrode with an area of 1 cm^2 was illuminated using a 1 kW xenon lamp from which infrared wavelengths were filtered by water, and wavelengths below 420 nm were cut off by an optical filter for measurements under visible light. The measured light irradiance by a thermopile detector was 100 mW/cm^2.

Results and discussion

Fig. 1(a) and (b) show FE-SEM images of TiO_2 nanorods and CuO nanoflake electrodes, respectively. A cross-section image of the TiO_2 nanorods shows that nanorods are grown nearly perpendicular to the FTO surface.

From the surface view of the TiO_2 nanorods, as shown in the inset of Fig. 1(a), we can see that individual nanorods have a rectangular shape. Fig. 1(b) shows the cross-sectional view of the CuO nanoflakes on the FTO substrate. The thickness of the CuO layer is ~2.2 μm, which can be controlled by varying the hydrothermal reaction time. Bright-field TEM analysis of the TiO_2 nanorods shown in Fig. 1(c) revealed that nanorods have smooth walls with a constant width of ~50 nm. The selected area diffraction pattern (SAD) and high-resolution TEM (HRTEM) image of a nanorod confirmed that it is a single crystalline, as shown in the inset of Fig. 1(c). Lattice fringes with an inter-planar spacing of $d_{(110)} = 3.2$ Å correspond with the rutile phase of the TiO_2.

Formation of nanoparticles on the surface of TiO_2 nanostructures was confirmed by HR-TEM analysis, as shown in the lower inset of Fig. 1(c). It is clearly seen that CdS and CdSe nanoparticles are present on the surface of the TiO_2. The lattice parameters of the nanoparticles were measured in the lattice fringes to be 0.356 and 0.255 nm, corresponding to the (100) and (102) of CdS and CdSe, respectively. Energy-dispersive X-ray spectroscopy (EDS) shown in Fig. S1 further confirm the existence of the CdS nanoparticles on the TiO_2 NRs. Fig. 1(d) shows the TEM results of the CuO nanoflakes. Fig. 2 shows the X-ray diffraction (XRD) analysis of the CuO nanoflake and TiO_2-nanorod electrodes. As-prepared CuO nanoflakes exhibit a polycrystalline nature with corresponding CuO diffraction peaks of (11), (111), and (020). The XRD result of the TiO_2 nanorods confirms the result obtained from TEM analysis—nanorods are single-crystalline with a dominant rutile phase.

Furthermore, before testing the combined operation of both electrodes, their photocatalytic properties were examined separately, as shown in Fig. 3. As an n-type electrode (photoanode), we have employed three types of TiO_2-nanorod-based electrodes, bare TiO_2 nanorods, CdS/CdSe-sensitized TiO_2 nanorods, and CdS/CdSe-sensitized TiO_2 nanorods with subsequent heat treatment (TiO_2CdS/CdSe-HT). As mentioned in the experimental section, both CdS and CdSe nanoparticles were subsequently deposited by SILAR method. First CdS nanoparticles layer was deposited for 15 SILAR cycles which formed CdS nanoparticles with an average size of 11 nm and density of 0.35 nanoparticles per 100 nm^2. Then TiO_2/CdS electrode was used to deposit CdSe for 5 SILAR cycles, thus forming final TiO_2/CdS/CdSe structure. Effect of the SILAR cycle number on the photocurrent response of the TiO_2 electrodes can be seen in Fig. S2. It can be seen that photocurrent response of the TiO_2 electrode is increasing with increase of SILAR number.

The electrodes are designated as A-1 (TiO_2-nanorod), A-2 (TiO_2CdS/CdSe), and A-3 (TiO_2CdS/CdSe-HT), respectively. The detailed study of bare and sensitized TiO_2 nanorods as well as the effect of post-heat treatment have been described in our previous studies [21]. It was demonstrated that the post-heat treatment of TiO_2/CdS/CdSe electrodes have improved its photocatalytic properties, owing to the increased crystallinity of the CdS/CdSe nanoparticles and their interface with TiO_2 nanorods.

Fig. 3(a) shows that the three photoanodes exhibit an anodic photocurrent, which confirms their n-type nature. As expected, the A-3 photoanode demonstrates the highest

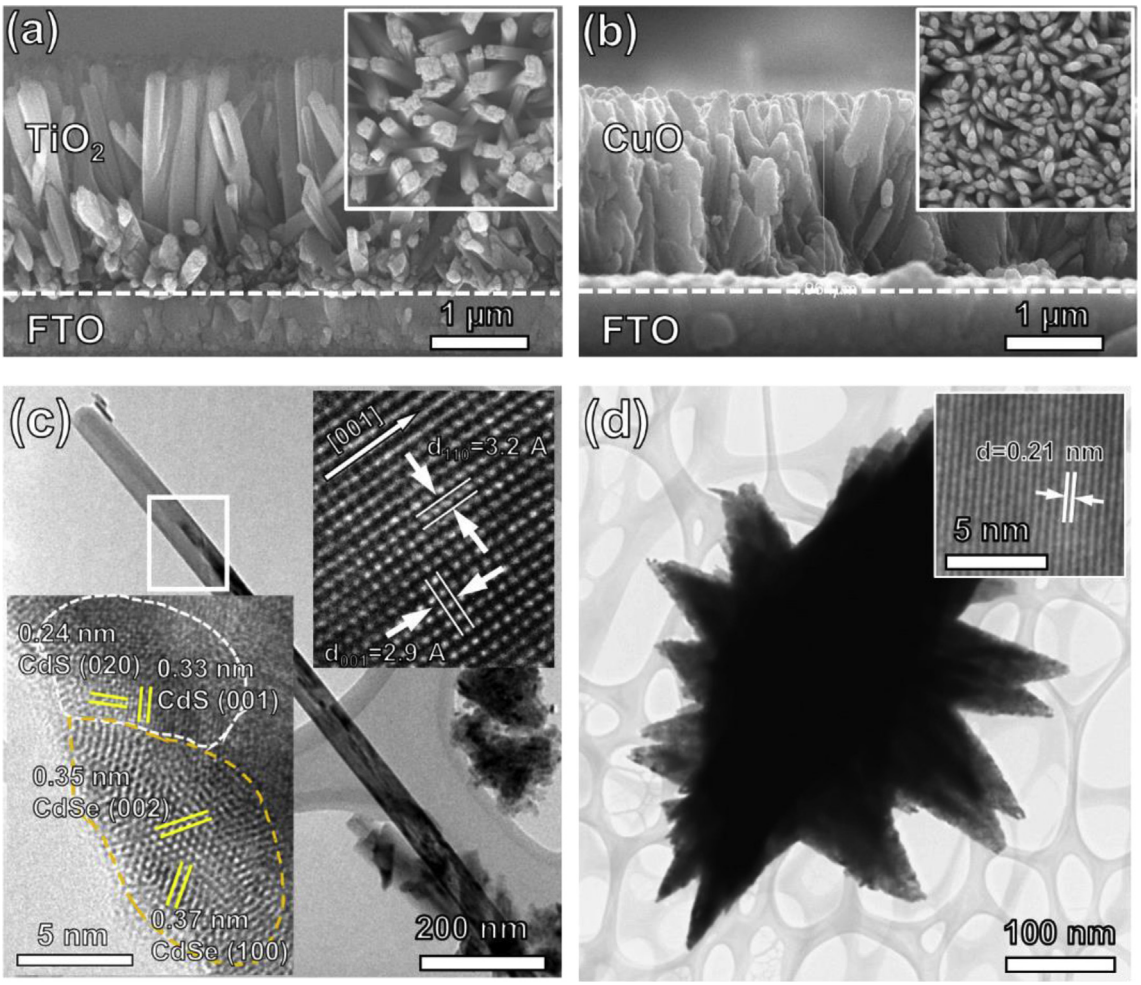

Fig. 1 – Morphological and structural analysis results of the TiO_2 nanorods and CuO nanoflakes. Cross-sectional SEM images of the (a) TiO_2 nanorods and (b) CuO photoelectrodes. Insets of each image shows surface views of TiO_2 and CuO. Bright-field TEM and HRTEM image of the (c) TiO_2/CdS/CdSe and (d) CuO nanostructures.

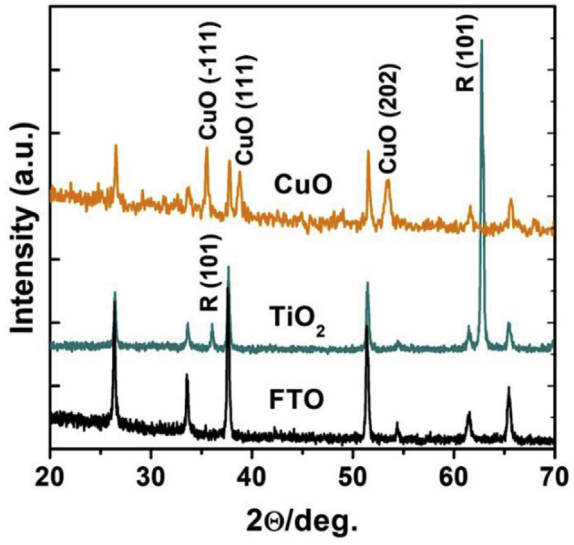

Fig. 2 – XRD patterns of the CuO nanoflakes and TiO_2-nanorod-based photoelectrodes.

photocurrent under white-light illumination. The visible-light performance of the electrodes are shown in Fig. S3 as the incident photon to current conversion efficiency (IPCE). Results indicate that CdS/CdSe sensitization of the TiO_2 nanorod has greatly improved its efficiency under visible light. Photocurrent–voltage measurements of the CuO electrode (designated as C1) shows a typical cathodic photocurrent response at negative voltages, confirming its p-type conductivity, as shown in Fig. 3(b). Maximum photocurrent densities of about 1.2 mA/cm^2 and 0.9 mA/cm^2 at 0.5 V (vs Ag/AgCl) were obtained under white- and visible-light illuminations, respectively.

It can be seen that photocurrent densities under both types of illumination are almost similar, due to the fact that CuO has a low bandgap (~1.7eV) [23] and absorbs a large portion of the visible-light spectrum (see UV–Vis absorbance spectra of the CuO in Fig. 5(a)). However, the photocorrosion of visible-light-active p-type photoelectrodes still remains an issue [24,25]. During the short period of light illumination (a couple of minutes during photocurrent measurements), photocorrosion of the CuO under light illumination is negligible, and its stability

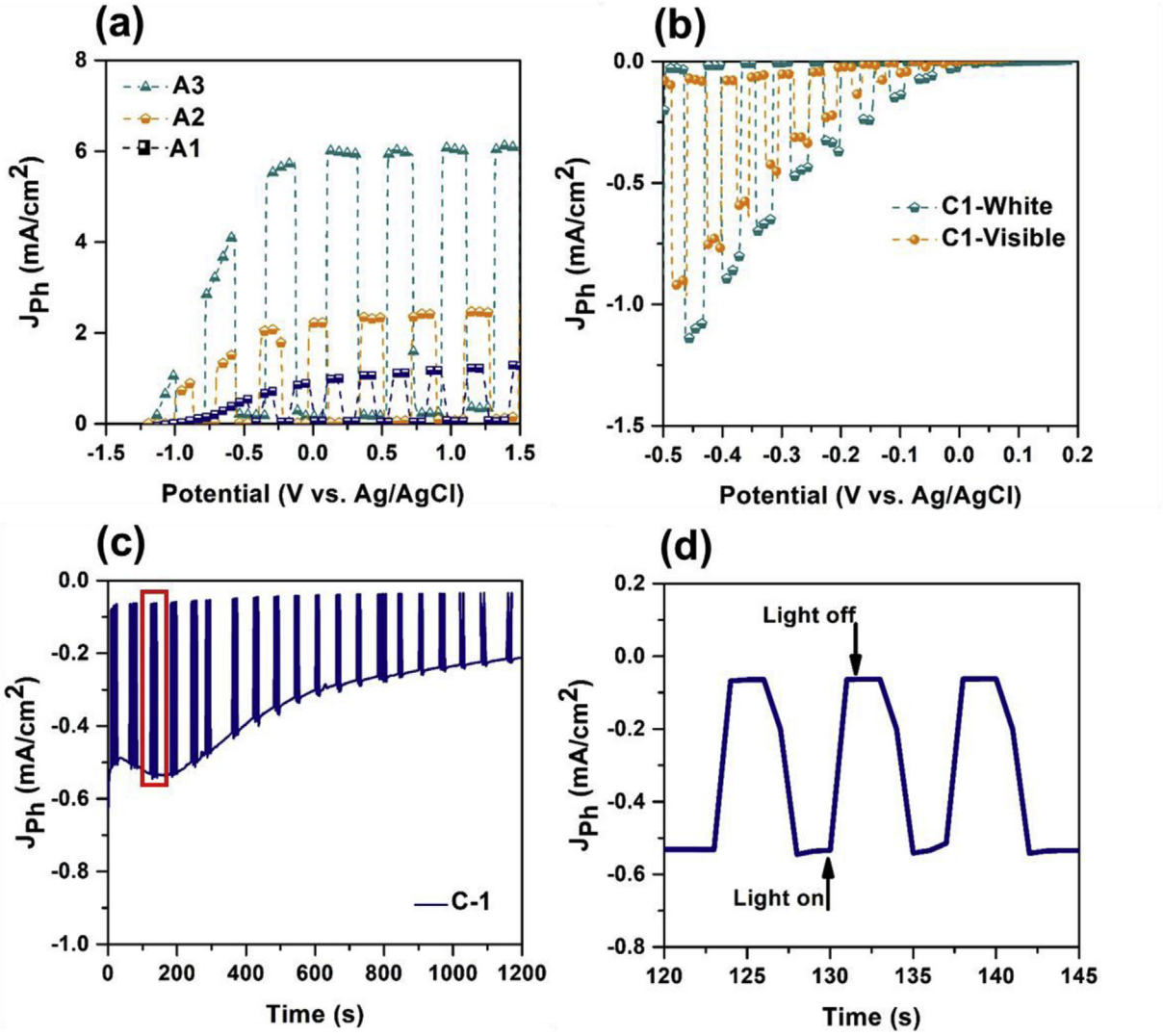

Fig. 3 – (a) Photocurrent density of the TiO_2-nanorod-based photoanodes. (b) Photocurrent density of the bare CuO electrode under white and visible light illuminations. (c) Stability (transient current density) results of the bare CuO photocathode at −0.5 V vs Ag/AgCl under illumination. (d) Enlarged view of the boxed area from (c).

cannot be judged accordingly. Therefore, photocurrent–time measurements were performed at −0.5 V vs Ag/AgCl for an extended period of time (stability measurement), as shown in Fig. 3(c). The result shows that the photocurrent of bare CuO electrode starts to decline after several minutes and continuously decreases until the end of the measurement. During the measurement, the illuminating light was periodically chopped. Fig. 3(d) shows an enlarged view of the current density from the boxed area of Fig. 3(c), where the chopping region is clearly demonstrated.

Careful observation of the photocurrent profile, shown in Fig. 3(c), indicates that photocurrent slightly increases at the beginning of the measurement and continuously declines. It is estimated that initial increase in photocurrent is due to charge releasing from trap in CuO as well as decrease of solution resistance by both diffusion and migration of reactive redox chemical species in electrolyte toward CuO electrode surface until establishing chemical equilibrium (same concentrations of electrode surface and bulk electrolyte). Subsequent decrease of the photocurrent density is associated with a photocorrosion of the CuO (photo-induced electrons are consumed to decompose CuO).

The morphology of the bare CuO nanostructured electrode after the stability measurement (Fig. 3(c)) was analyzed with FE-SEM and shown in Fig. S4. Figure S4 shows the cross-section and surface views of the CuO nanostructured electrode before and after stability measurement tests. It is clearly seen that the surface of the electrode after the measurement (Fig. S4(c and d)) has been completely destroyed, losing its nanostructured morphology after the stability measurement.

It is well known that oxides of Cu, such as CuO and Cu_2O, have photocorrosion issues, in which CuO decomposes under light illumination in aqueous media. The photocorrosion of CuO or Cu_2O occurs because the decomposition potential of CuO lies near or within the bandgap of CuO. Therefore, under light illumination, photo-excited electrons readily reduce CuO

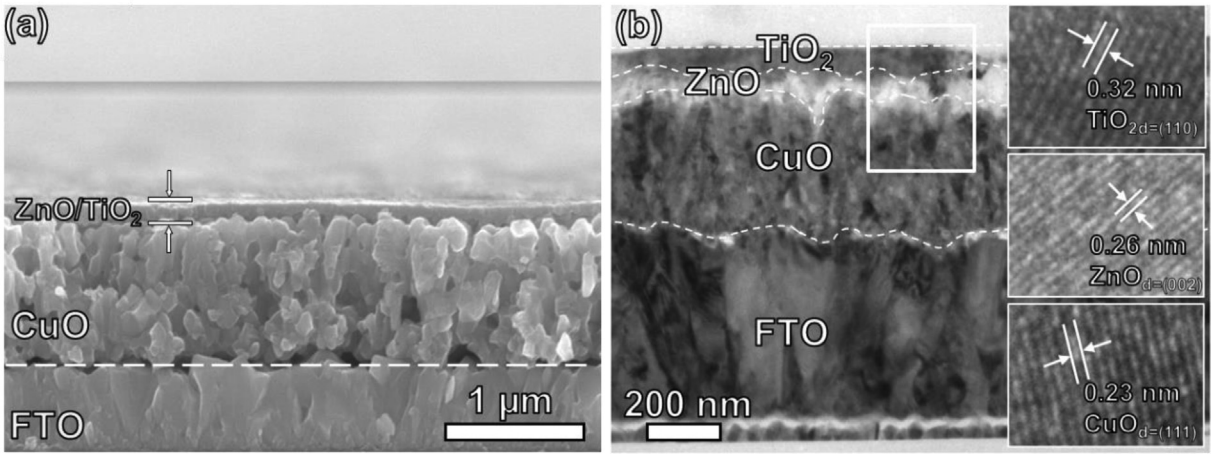

Fig. 4 – Morphology and microstructural characterization results of the ZnO/TiO_2 thin film coated CuO electrode. (a) Cross-sectional FE-SEM images of the FTO/CuO/ZnO/TiO_2 electrode. (b) Cross-sectional bright-field TEM image of the FTO/CuO/ZnO/TiO_2 electrode. Inset of the of the (b) shows HRTEM results of each TiO_2, ZnO and CuO layers obtained from the white boxed regions.

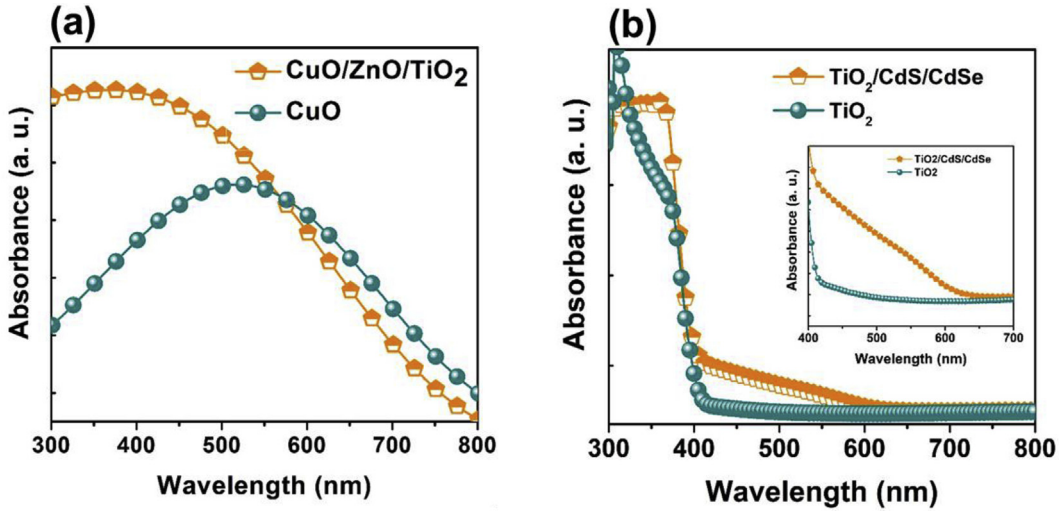

Fig. 5 – UV–Vis absorbance spectra of the (a) bare CuO and CuO/ZnO/TiO_2 electrodes. (b) Absorbance spectra of the bare TiO_2 and TiO_2/CdS-HT/CdSe-HT electrodes.

rather than hydrogen protons according to following equation [25]:

$$CuO + H_2O + 2e^- \leftrightarrow Cu + 2OH^- \quad (1)$$

Therefore, photocorrosion of CuO has been extensively studied and a number of reasonable strategies have been developed. Several studies have reported that coating CuO with a layer of suitable protecting material greatly improves its stability [24,26–28]. Paracchino et al. reported that the coating of Cu_2O electrode with Al:ZnO/TiO_2/Pt layers by atomic layer deposition (ALD) greatly improves both the stability and photocatalytic properties of the electrode [19]. Similarly, in this work, CuO electrode was subsequently coated with ZnO and TiO_2 layers, forming a ZnO/TiO_2 double layer; however, we employed a conventional, low-cost, spin-coating method instead of atomic layer deposition. Here, ZnO layer plays a dual role: (i) it forms favorable intermediate path for photo-induced electrons as schematically shown in Fig S5 (a) and (ii) it provides smooth foundation before TiO_2 deposition, filling up the uneven morphology of the CuO surface (Fig S5 (b)). Thus, much smoother TiO_2 layer could be deposited. Fig. 4(a) shows cross-sectional FE-SEM images of the CuO electrode after it was spin-coated with ZnO/TiO_2 film. From the cross-section image of the electrode, we can clearly see the coated layer on top of the CuO nanostructured film, with a thickness of 80 nm. Furthermore, the coating quality and crystalline state of the coated layers have been examined by TEM analysis. Cross-sectional TEM specimen have been prepared by the focused ion beam method from the FTO/CuO/ZnO/TiO_2 sample. The cross-sectional TEM image revealed that ZnO/TiO_2 is well distributed on the CuO surface. Bright-

field TEM images (Fig. 4(b)) confirm the expected structure of the electrode, FTO/CuO/ZnO/TiO_2, with a ZnO/TiO_2 layer thickness of approximately 80 nm, which agrees well with the FE-SEM results.

By close examination of the interface of CuO/ZnO/TiO_2, it was found that the ZnO layer consists of randomly deposited nanoparticles, rather than continuous film. To confirm the exact composition of each layer, an HRTEM analysis has been carried out from each corresponding layer (white box area), as shown in the inset of Fig. 4(b).

To explore the optimum thickness of the protecting layer, electrodes with different ZnO/TiO_2 layer thicknesses have been tested. The thickness of the TiO_2 layer was controlled by changing the spin-coating number, while maintaining the ZnO layer thickness constant. Figure S6 shows the cross-sectional FE-SEM results of the CuO electrodes coated with different TiO_2 layer thicknesses. The TiO_2 spin-coating number varied from 3 to 9 at 3000 rpm, and the corresponding thickness of the TiO_2 layer was changed from 100 to 400 nm, respectively. However, by increasing the thickness of the TiO_2 layer above 250 nm, the quality and adhesion of the film became poor (coated film starts to lift off), as can be seen from Fig. S6 (d). We believe that the initially highly rough surface of CuO and the interfacial stress at the CuO:ZnO/TiO_2 layer can cause the lift-off problem at larger thicknesses.

Optical properties of both electrodes were analyzed by UV–vis spectroscopy and shown in Fig. 5. The CuO electrode absorbs a wide range of visible light, up to the wavelength of 850 nm, which corresponds to the bandgap of 1.5 eV, as shown in Fig. 5(a). The absorbance edge decreased to 770 nm after the coating with the ZnO/TiO_2 layer; however, the absorbance in the UV region was enhanced most probably because of the wide bandgap of the ZnO/TiO_2 layer. On the other hand, bare TiO_2 nanorods, as expected, show an absorption edge up to 400 nm, and after sensitization with CdS/CdSe, its absorption edge is red shifted to the visible-light region of the spectrum, up to 700 nm (Fig. 5(b)). It can be concluded that both electrodes are active under visible light. Fig. 6 shows the photocurrent measurement results of the CuO sample after coating with a ZnO/TiO_2 protective layer, in which the thickness of the TiO_2 film varied as 100 nm, 150 nm, and 200 nm. The electrodes were designated as C-1 (CuO), C-2 (CuO/ZnO/TiO_2 (100 nm)), C-3 (CuO/ZnO/TiO_2 (150 nm)), and C-4 (CuO/ZnO/TiO_2 (200 nm)). The results shown in Fig. 6(a) reveal that the

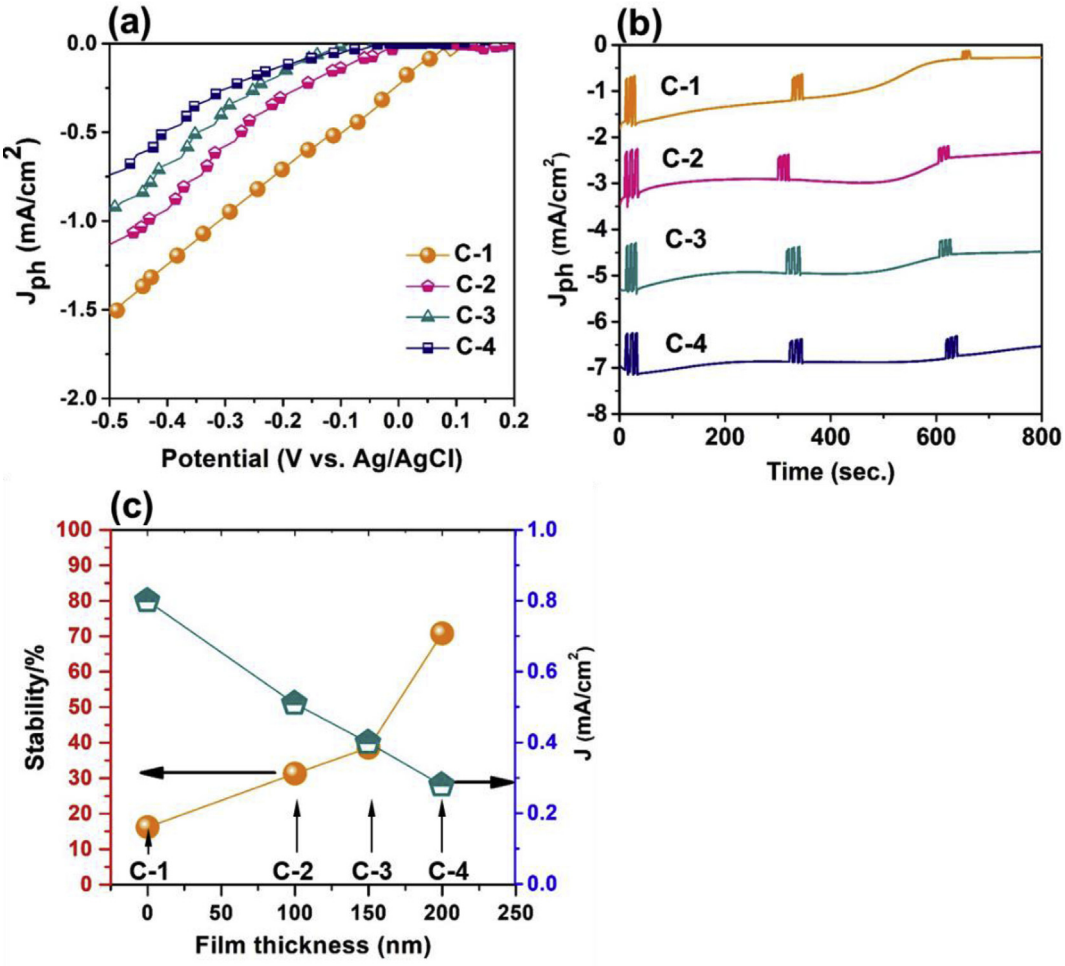

Fig. 6 – Photoelectrochemical characterizations of the C-1, C-2, C-3, and C-4 photocathodes. (a) Photocurrent response of the photocathodes (C-1, C-2, C-3, and C-4) in 0.1 M KOH electrolyte. (b) Dependence of the stability and remnant photocurrent on the thickness of the ZnO/TiO_2 protecting layer. (c) Dependence of the photocathodes performance on the protecting layer's thickness.

photocurrent values of the electrodes at −0.5 V vs Ag/AgCl decrease with an increase in the TiO_2 layer thickness. The highest photocurrent value corresponds to the bare CuO electrode.

The reduction in the photocurrent value of the electrodes with ZnO/TiO_2 protecting layers could be attributed to the fact that an additional layer may limit the absorption range of CuO, as well as cause additional charge transfer resistance at the electrode/electrolyte interface [29]. The stability of the electrodes, however, was increased by increasing the thickness of the TiO_2 layers, as can be seen from the stability measurement results shown in Fig. 6(b). Fig. 6 (b) shows the photocurrent profiles of four photoelectrodes (C-1, C-2, C-3, C-4) measured in chronoamperometry mode for stability test, where photocurrent was measured at fixed potential (−0.5 V vs. Ag/AgCl) for extended period of time. It is basically identical measurement as shown in Fig. 3(c). In Fig. 3(c) the light source was continuously chopped throughout the measurement. In case of Fig. 6 (b), the light source was chopped occasionally, at the beginning of the measurement, at the middle and at the end of the measurement. Stability of the electrodes was quantified as the percentage of the remnant photocurrent density at the beginning of the measurement, compared with that at the end of the measurement. The remnant photocurrent was determined from the chopped photocurrent, by subtracting the photocurrent at "light on" from the photocurrent at "light off". Fig. 6(c) shows the dependence of the stability and remnant photocurrent density of the electrodes on the protective film thickness. The stability of the C-1, C-2, C-3, and C-4 electrodes were 16.2%, 31.3%, 38.6%, and 70.8%, respectively. This demonstrates that coating the electrodes with TiO_2 film strongly enhances the stability of the photoelectrodes. Furthermore, both n-type and p-type photoelectrodes were short-circuited in the H-type photocell to evaluate their combined operation. Two compartments of the H-type cell were separated by a Nafion membrane as shown in Fig. 7(a). The electrolyte in the n-type and p-type sides of the cell were 0.1 M Na_2S and 0.1 KOH, respectively, and their pH values were adjusted to be equal to eliminate chemical bias caused by the pH difference. Fig. 7(b) shows the band diagrams of both electrodes in the short-circuited state. Theoretically, when a semiconductor is in

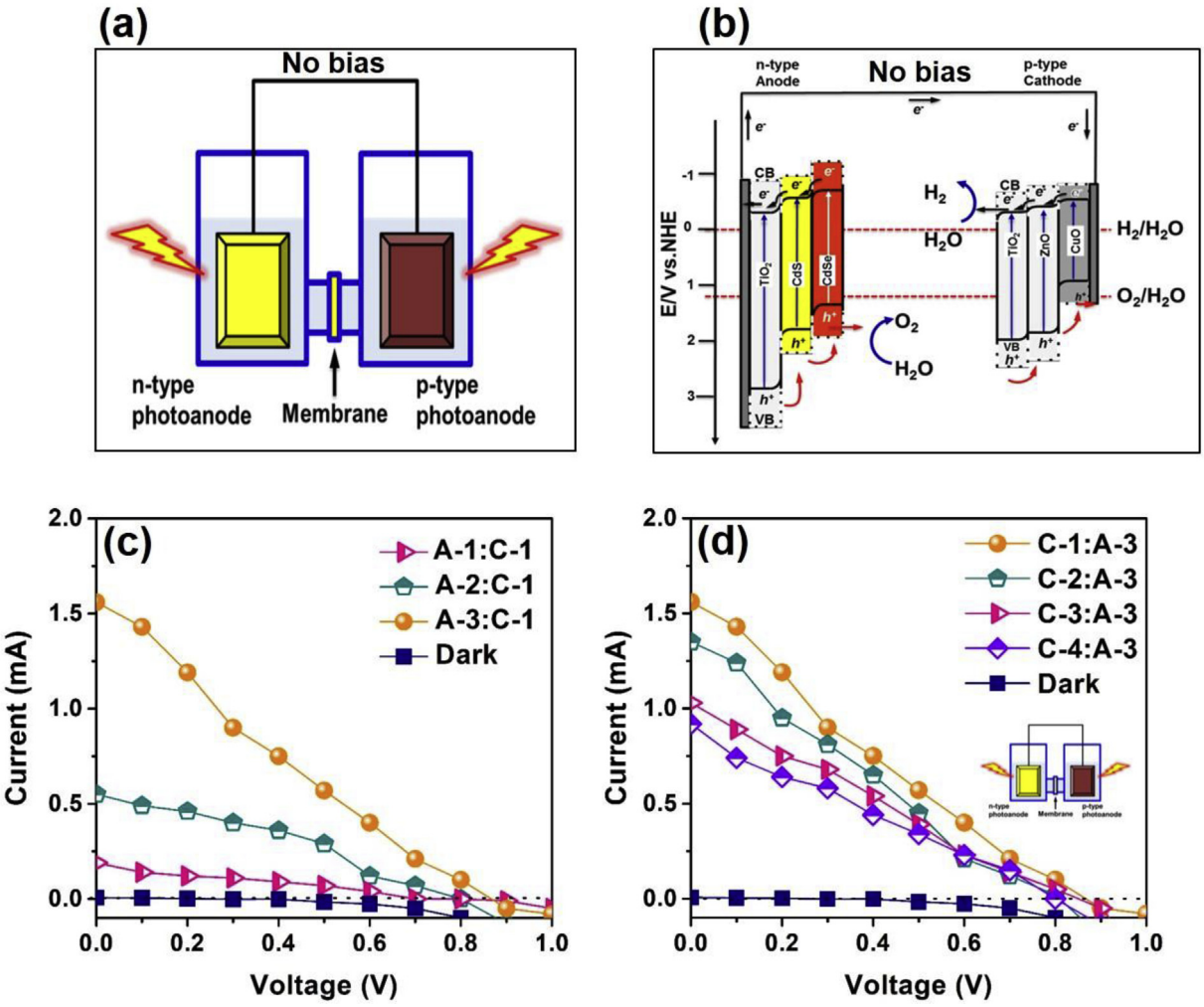

Fig. 7 – Schematic illustration (a) and band diagram (b) of the photocell consisting of n-TiO_2 and *p*-CuO-based photoelectrodes. (c) I–V curves of the photocell with fixed C-1 photocathode and A-1, A-2, and A-3 photoanodes. (d) I–V curves of the photocell with fixed A-3 photoanode and C-1, C-2, C-3, and C-4 photocathodes.

contact with an aqueous electrolyte, its bands bend upward or downward for n-type and p-type semiconductors, respectively. Hence, photogenerated electrons in a p-type CuO electrode reduces the water to hydrogen, and holes in the n-type TiO_2 oxidize the water to oxygen, when both electrodes are illuminated by light with a photon energy greater than their bandgap. The current–voltage (I–V) characterization of the photocell is an important measurement that reveals if the studied photoelectrodes can operate effectively together.

Moreover, performance of the photocell at various photocathode/photoanode configurations was tested to investigate the effect of each electrode and their suitable configuration. Fig. 7(c) shows I–V curves of the photocell with fixed C-1 photocathode and different photoanodes (A-1, A-2, A-3, A-4) under dark and light illumination without external bias. The open circuit voltage (OCV) of the cell is 0.803 V, and the short-circuit current (J_{SC}, V = 0 V) values are 0.19 mA, 0.55 mA, and 1.56 mA for A-1, A-2, and A-3 electrodes, respectively. The highest and lowest observed value of J_{sc} corresponds to the TiO_2CdS/CdSe-HT and bare TiO_2 electrodes, which demonstrated behavior similar to the photocurrent measurement shown in Fig. 3(a). The current–voltage results indicate that the J_{sc} value of the photocell strictly depends on the PEC properties of the electrodes.

Fig. 7(d) shows the I–V curves of the photocell with fixed A-3 photoanode and different photocathodes (C-1, C-2, C-3, C-4). The obtained results show that the J_{sc} value of the photocell with bare CuO photocathode exhibits the highest J_{sc} value, which linearly decreases according to the thickness of the protecting layer of the employed photocathode. This behavior is similar to the photocurrent density results given in Fig. 6(a).

Finally, from the I–V curve results shown in Fig. 7(d) we have calculated the photoconversion efficiency of our self-driven photocell by using the following equation given in Ref. [14]:

$$\eta = \left[\frac{(J_{sc} \times E^0_{rev})}{2I_0}\right] \times 100 \quad (2)$$

where J_{sc} is the short circuit current, E^0_{rev} is the standard reversible potential (1.23 V/NHE) for the water-splitting reaction, and I_0 is the intensity of the illuminating light.

Photocell performance with all electrode configurations is summarized in Table 1. Clearly, the photocell with A-3 and C-1 electrodes has the highest efficiency of 0.96%, while the photocell with the most stable C-4 electrode (C-4:A-3) has an efficiency of 0.57%. The obtained efficiency of 0.57% of the photocell with C-4:A-3 electrode configuration is almost an order of magnitude higher than the similar self-sustaining photocell reported in ref [12,13], in which a photocell with n-TiO_2 and p-SiC photoelectrodes exhibited a photoconversion efficiency of 0.06%. The improved performance of our photocell was attributed to the fact that both photoelectrodes used in our work were highly active in the visible-light region of the solar spectrum. In contrast, both n-TiO_2 (3.2 eV) and p-SiC (3 eV) have large bandgaps; thus, they are less active in the visible-light region of the spectrum.

Finally, from the I–V curve measurement results shown in Fig. 7(c) and (d), we can conclude that the J_{sc} value of the photocell strictly depends on the photocatalytic properties of the individual employed photoelectrodes. Operation conditions of a photocell without external voltage could be evaluated by intersecting the photocurrent density–potential (J–V) curves of the photoanode and photocathode with metal counter electrode. The maximum operation current density for the photocell lies at the intersection point of the two J–V curves. The absence of the intersection point of the two J–V curves means insufficient driving force for the photoelectrolysis of water [24–26].

Fig. S7 shows J–V curves for the A-3 photoanode from Fig. 3(a) and C-4 photocathode from Fig. 6(a). The intersection point of the two curves was measured as approximately ~1.5 mA/cm^2. Thus the photocell consisting of the A-3 photoanode and C-4 photocathode can be operated without external bias for photocatalytic water splitting.

Furthermore, in general, OCV of the photocell can be expressed as a difference between the fermi levels of n-type photoanode and p-type photocathode. The difference between the two onset potentials of photoanode and photocathode is almost the same as the OCV value of the photocell [13]. The onset potential is corresponding to the required voltage for triggering photocatalytic response current. In our case, the onset potentials of the TiO_2-based A-3 photoanode with the highest photocurrent density and CuO-based C-4 photocathode with the most stability are −1.15 V and −0.045 V, respectively. Thus the onset potential difference was 1.1 V, which was close to the OCV 0.8 V measured for the

Table 1 – Performance parameters of the photocell with different n-and p-type photoelectrode configurations.

Electrode	J_{scc} (mA)	V_{oc} (V)	η (%)
C-1:A-3	1.56	0.9	0.96
C-2:A-3	1.35	0.85	0.83
C-3:A-3	1.03	0.8	0.64
C-4:A-3	0.92	0.8	0.57

photocell with C-4/A-3 configuration (see Fig. 7(d)). This implies that the chosen photoelectrode combination can be successfully operated in a tandem structure for photocatalytic water splitting. Further enhancement of the solar-to-hydrogen conversion efficiency of the system could be achieved by reducing the over potential of the electrodes by employing a suitable co-catalysts for oxygen evolution and hydrogen evolution reactions [30].

Summary

We have successfully prepared a CuO nanostructured film on a transparent electrode as a p-type photocathode to employ in a self-sustaining photocell. The photocorrosion of the CuO electrode was suppressed by coating with a 200-nm-thick ZnO/TiO_2 protective layer and demonstrated over 70% stability under light illumination. The $CuO/ZnO/TiO_2$ electrode was employed in the photocell together with an n-type TiO_2-based electrode. It was found that the photoconversion efficiency of the photocell strongly depends on the photocatalytic properties of the individual photoelectrodes. The photocell with the highly stable photocathode $CuO/ZnO/TiO_2$ and effective n-type TiO_2/CdS/CdSe-HT photoanode have demonstrated a photoconversion efficiency of 0.57%, which is much higher than that from previous studies. We conclude that the photocell consisting of visible-light-active p-type CuO and n-type TiO_2/CdS/CdSe-HT photoelectrodes can operate without external bias under visible-light illumination.

Acknowledgement

This paper was supported by Kumoh National Institute of Technology.

Appendix A. Supplementary data

Supplementary data to this article can be found online at https://doi.org/10.1016/j.ijhydene.2019.12.052.

REFERENCES

[1] Finegold L, Cude JL. Biological sciences: one and two-dimensional structure of alpha-helix and beta-sheet forms of poly(L-Alanine) shown by specific heat measurements at low temperatures (1.5-20 K). Nature 1972;238:38–40. https://doi.org/10.1038/238038a0.
[2] Kudo A, Miseki Y. Heterogeneous photocatalyst materials for water splitting. Chem Soc Rev 2009;38:253–78. https://doi.org/10.1039/b800489g.
[3] Prévot MS, Sivula K. Photoelectrochemical tandem cells for solar water splitting. J Phys Chem C 2013;117:17879–93. https://doi.org/10.1021/jp405291g.
[4] Brillet J, Yum J-H, Cornuz M, Hisatomi T, Solarska R, Augustynski J, et al. Highly efficient water splitting by a dual-absorber tandem cell. Nat Photonics 2012;6:824–8. https://doi.org/10.1038/nphoton.2012.265.
[5] Fan K, Li FS, Wang L, Daniel Q, Gabrielsson E, Sun LC. Pt-free tandem molecular photoelectrochemical cells for water splitting driven by visible light. Phys Chem Chem Phys 2014;16:25234–40. https://doi.org/10.1039/c4cp04489d.
[6] Abdi FF, Han L, Smets AHM, Zeman M, Dam B, van de Krol R. Efficient solar water splitting by enhanced charge separation in a bismuth vanadate-silicon tandem photoelectrode. Nat Commun 2013;4:2195. https://doi.org/10.1038/ncomms3195.
[7] Xu K, Chatzitakis A, Vøllestad E, Ruan Q, Tang J, Norby T. Hydrogen from wet air and sunlight in a tandem photoelectrochemical cell. Int J Hydrogen Energy 2019;44:587–93. https://doi.org/10.1016/j.ijhydene.2018.11.030.
[8] Yin X, Liu Q, Yang Y, Liu Y, Wang K, Li Y, et al. An efficient tandem photoelectrochemical cell composed of FeOOH/TiO 2/BiVO 4 and Cu 2 O for self-driven solar water splitting. Int J Hydrogen Energy 2019;44:594–604. https://doi.org/10.1016/j.ijhydene.2018.11.032.
[9] Maeda K. Z-scheme water splitting using two different semiconductor photocatalysts. ACS Catal 2013;3:1486–503. https://doi.org/10.1021/cs4002089.
[10] Abe R. Recent progress on photocatalytic and photoelectrochemical water splitting under visible light irradiation. J Photochem Photobiol C Photochem Rev 2010;11:179–209. https://doi.org/10.1016/j.jphotochemrev.2011.02.003.
[11] Park HS, Lee HC, Leonard KC, Liu G, Bard AJ. Unbiased photoelectrochemical water splitting in Z-scheme device using W/Mo-doped BiVO4 and ZnxCd1-xSe. ChemPhysChem 2013;14:2277–87. https://doi.org/10.1002/cphc.201201044.
[12] Ida S, Yamada K, Matsunaga T, Hagiwara H, Matsumoto Y, Ishihara T. Preparation of p-type CaFe2O4 photocathodes for producing hydrogen from water. J Am Chem Soc 2010;132:17343–5. https://doi.org/10.1021/ja106930f.
[13] Ida S, Yamada K, Matsuka M, Hagiwara H, Ishihara T. Photoelectrochemical hydrogen production from water using p-type and n-type oxide semiconductor electrodes. Electrochim Acta 2012;82:397–401. https://doi.org/10.1016/j.electacta.2012.03.174.
[14] Akikusa J. Photoelectrolysis of water to hydrogen in p-SiC/Pt and p-SiC/n-TiO2 cells. Int J Hydrogen Energy 2002;27:863–70. https://doi.org/10.1016/S0360-3199(01)00191-4.
[15] Tilley SD. Recent advances and emerging trends in photo-electrochemical solar energy conversion. Adv Energy Mater 2019;9:1–13. https://doi.org/10.1002/aenm.201802877.
[16] Wang Z, Li C, Domen K. Recent developments in heterogeneous photocatalysts for solar-driven overall water splitting. Chem Soc Rev 2019;48:2109–25. https://doi.org/10.1039/c8cs00542g.
[17] Sharma S, Pai MR, Kaur G, Divya, Satsangi VR, Dass S, et al. Efficient hydrogen generation on CuO core/Ag–TiO 2 shell nano-hetero-structures by photocatalytic splitting of water. Renew Energy 2019;136:1202–16. https://doi.org/10.1016/j.renene.2018.09.091.
[18] Bagtache R, Saib F, Abdmeziem K, Trari M. A new hetero-junction p-CuO/Al2O3 for the H2 evolution under visible light. Int J Hydrogen Energy 2019;44:22419–24. https://doi.org/10.1016/j.ijhydene.2019.01.109.
[19] Lee HJ, Bang J, Park J, Kim S, Park SM. Multilayered semiconductor (CdS/CdSe/ZnS)-sensitized TiO2 mesoporous solar cells: all prepared by successive ionic layer adsorption and reaction processes. Chem Mater 2010;22:5636–43. https://doi.org/10.1021/cm102024s.
[20] Chi CF, Liau SY, Lee YL. The heat annealing effect on the performance of CdS/CdSe-sensitized TiO2 photoelectrodes in photochemical hydrogen generation. Nanotechnology 2010;21. https://doi.org/10.1088/0957-4484/21/2/025202.

[21] Shaislamov U, Yang BL. Single crystalline TiO2 nanorods with enhanced visible light activity for solar hydrogen generation. Int J Hydrogen Energy 2013;38. https://doi.org/10.1016/j.ijhydene.2013.08.045.
[22] Shaislamov U, Yang BL. CdS-sensitized single-crystalline TiO2 nanorods and polycrystalline nanotubes for solar hydrogen generation. J Mater Res 2013;28. https://doi.org/10.1557/jmr.2012.373.
[23] Chiang CY, Chang MH, Liu HS, Tai CY, Ehrman S. Process intensification in the production of photocatalysts for solar hydrogen generation. Ind Eng Chem Res 2012;51:5207–15. https://doi.org/10.1021/ie202522g.
[24] Tilley SD, Schreier M, Azevedo J, Stefik M, Grätzel M. Ruthenium oxide hydrogen evolution catalysis on composite cuprous oxide water splitting photocathodes. Adv Funct Mater 2014;24:303–11. https://doi.org/10.1002/adfm201301106.
[25] Paracchino A, Laporte V, Sivula K, Grätzel M, Thimsen E. Highly active oxide photocathode for photoelectrochemical water reduction. Nat Mater 2011;10:456–61. https://doi.org/10.1038/nmat3017.
[26] Wang P, Zhao X, Li B. ZnO-coated CuO nanowire arrays: fabrications, optoelectronic properties, and photovoltaic applications. Opt Express 2011;19:11271–9. https://doi.org/10.1364/OE.19.011271.
[27] Kargar A, Jing Y, Kim SJ, Riley CT, Pan X, Wang D, et al. ZnO/CuO heterojunction branched. 2013. p. 11112–20.
[28] Azevedo J, Steier L, Dias P, Stefik M, Sousa CT, Araújo JP, et al. On the stability enhancement of cuprous oxide water splitting photocathodes by low temperature steam annealing. Energy Environ Sci 2014;7:4044–52. https://doi.org/10.1039/C4EE02160F.
[29] Shaislamov U, Krishnamoorthy K, Kim SJ, Chun W, Lee H-J. Facile fabrication and photoelectrochemical properties of a CuO nanorod photocathode with a ZnO nanobranch protective layer. RSC Adv 2016;6. https://doi.org/10.1039/c6ra18832j.
[30] Bornoz P, Abdi FF, Tilley SD, Dam B, Van De Krol R, Graetzel M, et al. A bismuth vanadate – cuprous oxide tandem cell for overall solar water splitting. 2014.